Journal of Catalysis 269 (2010) 80–92

Contents lists available at ScienceDirect

Journal of Catalysis

journal homepage: www.elsevier.com/locate/jcat

Partial hydrogenation of propyne over copper-based catalysts and comparison with nickel-based analogues

Blaise Bridier [a], Núria López [a], Javier Pérez-Ramírez [a,b,*]

[a] Institute of Chemical Research of Catalonia (ICIQ), Avinguda Països Catalans 16, 43007 Tarragona, Spain
[b] Catalan Institution for Research and Advanced Studies (ICREA), Passeig Lluís Companys 23, 08010 Barcelona, Spain

ARTICLE INFO

Article history:
Received 5 September 2009
Revised 21 October 2009
Accepted 23 October 2009
Available online 8 December 2009

Keywords:
Partial hydrogenation
Alkyne
Alkene
Oligomers
Copper
Nickel
Hydrotalcite
Mechanism
DFT
Hydride

ABSTRACT

The partial hydrogenation of propyne was studied over copper-based catalysts derived from Cu–Al hydrotalcite and malachite precursors and compared with supported systems (Cu/Al_2O_3 and Cu/SiO_2). The as-synthesized samples and the materials derived from calcination and reduction were characterized by XRF, XRD, TGA, TEM, N_2 adsorption, H_2-TPR, XPS, and N_2O pulse chemisorption. Catalytic tests were carried out in a continuous flow-reactor at ambient pressure and 423–523 K using H_2:C_3H_4 ratios of 1–12 and were complemented by *operando* DRIFTS experiments. The propyne conversion and propene selectivity correlated with the copper dispersion, which varied with the type of precursor or support and the calcination and reduction temperatures. The highest exposed copper surface was attained on hydrotalcite-derived catalysts, which displayed C_3H_6 selectivity up to 80% at full C_3H_4 conversion and stable performance in long-run tests at $T \geqslant 473$ K. Both activated Cu–Al hydrotalcites (this work) and Ni–Al hydrotalcites [S. Abelló, D. Verboekend, B. Bridier, J. Pérez-Ramírez, J. Catal. 259 (2008) 85] exhibited a relatively high alkene selectivity under optimal operation conditions, but they present a markedly distinctive catalytic behavior with respect to temperature and hydrogen-to-alkyne ratio. The product distribution was assigned through Density Functional Theory (DFT) simulations to the different stability of subsurface phases (carbides, hydrides) and the energies and barriers for the competing reaction mechanisms. The behavior of Cu in partial alkyne hydrogenation resembles that of Au nanoparticles, while Ni is closer to Pd.

1. Introduction

Light olefins, e.g. ethylene and propylene, generated by steam and fluid catalytic cracking, alkane dehydrogenation, and methanol to olefins, contain impurities of acetylenics and diolefins as by-products. Reducing the level of these highly unsaturated compounds to <5–10 ppm is required to fulfill the stringent specifications for both chemical and polymer-grade ethylene and propylene. The selective hydrogenation of alkynes and alkadienes to the corresponding mono-olefin is the most attractive option for upgrading alkene streams [1,2]. The standard catalyst in industry is palladium (<0.05 wt%) on low-surface-area alumina. Pd/Al_2O_3 modification by promoters (e.g. a second metal like Ag, Au, Pb, Cu, etc.) and/or additives (e.g. feeding of CO) is mandatory to increase both the alkene selectivity and catalyst lifetime [2–4]. These modifiers induce electronic and/or geometric effects on the palladium sites that reduce the extent of the two undesired reactions: over-hydrogenation to the alkane and oligomerization to higher hydrocarbons (green oil or fouling).

Recent work in the topic of partial alkyne hydrogenation has mostly focused on different aspects encircling palladium-based catalysts: novel preparation methods and supports [5–8], structure sensitivity of Pd nanoparticles [7], effect of modifiers [9,10], and selectivity-governing factors associated with the formation of hydride and carbide phases [11,12]. Catalysts based on other metals have been studied marginally. Several authors have shown and explained the highly selective character of supported gold nanoparticles in partial hydrogenation of alkynes [13,14]. In the search for a noble metal-free catalyst, Studt et al. [15] proposed, based on DFT calculations, nickel–zinc alloys for acetylene hydrogenation. Our group has reported high alkene selectivity of activated Ni–Al hydrotalcite (80%) in propyne and propadiene hydrogenation compared with conventional Ni/Al_2O_3 prepared by impregnation (30%) [16]. This was attributed to the unique features of the catalyst imposed by the hydrotalcite precursor, including *high* metal loadings, *high* metal interdispersion, and *high* surface area.

The hydrotalcite route for nickel [16] opens a way to improve the performance of metals traditionally regarded as *poor* partial hydrogenation catalysts. Copper is one of these metals. Early

* Corresponding author. Address: Institute of Chemical Research of Catalonia (ICIQ), Avinguda Països Catalans 16, 43007 Tarragona, Spain. Fax: +34 977 920 224.
E-mail address: jperez@iciq.es (J. Pérez-Ramírez).

0021-9517/$ - see front matter © 2009 Elsevier Inc. All rights reserved.
doi:10.1016/j.jcat.2009.10.019

alkyne hydrogenation studies by Bond and Mann [17] using a batch reactor reported low activity and high selectivity to oligomers of unsupported or supported copper catalysts compared to iron, cobalt, and nickel counterparts. Green oil formation caused rapid deactivation. Supported copper catalysts were studied in the 1990s by Trimm, Cant, and coworkers [18–21]. Silica or magnesia-supported copper catalysts were 30 times more active than unsupported copper and led to propene selectivity up to 80% at 550 K in propyne hydrogenation. Long-term tests were successfully conducted with an industrial raw feed containing 93% C_3H_6, 2% C_3H_4, and 5% C_3H_8 using a ratio H_2:C_3H_4 of 4 and temperatures >433 K [18]. Below 433 K, green oil formation caused fast catalyst deactivation. Later studies by Rodriguez et al. [22] also revealed strong deactivation of a reduced Cu–Zn–Al catalyst in C_2H_2 hydrogenation at 448 K. These authors concluded the low interest of copper compared to the reduced Ni–Zn–Al oxide.

Herein, we have studied the gas-phase hydrogenation of propyne over unpromoted Cu-based catalysts derived from hydrotalcite and malachite precursors as well as supported systems (Cu/SiO_2 and Cu/Al_2O_3). Detailed characterization, catalyst testing, and *operando* infrared spectroscopic studies show that a proper synthetic route and activation conditions are essential to make it possible for Cu-based catalysts to compete with Ni-based counterparts. The hydrogenation performance correlates well with the copper dispersion, which depends on the type of precursor or support and the calcination and reduction temperatures. The distinct catalytic behavior of activated Cu–Al and Ni–Al hydrotalcites in alkyne hydrogenation was concluded from tests at different temperatures and H_2:C_3H_4 ratios, as well as from analysis of oligomers at the reactor outlet. Complementary, mechanitic differences between copper and nickel were explained by Density Functional Theory (DFT) simulations.

2. Experimental

2.1. Catalyst preparation and activation

Cu–Al hydrotalcite with a nominal Cu/Al molar ratio of 3 was synthesized by continuous coprecipitation using the in-line deposition precipitation (ILDP) method [23]. Aqueous solutions of 0.75 M $Cu(NO_3)_2{\cdot}6H_2O$ and 0.25 M $Al(NO_3)_3{\cdot}9H_2O$ and the precipitating agent ($NaOH + Na_2CO_3$, 1 M of each) were pumped into a 6 cm^3-reactor attached to a high-shear homogenizer rotating at 13,500 rpm. The pH of the slurry was measured and controlled by an in-line probe directly at the outlet of the precipitation chamber. The coprecipitation was carried out at pH 9 with an average residence time of 18 s. The slurry was aged at 313 K for 12 h under mechanical stirring (500 rpm), followed by filtration, washing, and drying at 353 K for 12 h. Malachite was also synthesized using the ILDP method but excluding the aluminum salt from the cationic solution. The alumina and silica-supported copper catalysts (15 wt% Cu) were prepared by incipient wetness impregnation of γ-Al_2O_3 (Aldrich, type 507C, S_{BET} = 155 $m^2\,g^{-1}$) and pyrogenic SiO_2 (Riedel-de Haën, Cab-O-Sil® M5, S_{BET} = 200 $m^2\,g^{-1}$), respectively, with appropriate amounts of a $Cu(NO)_3{\cdot}6H_2O$ aqueous solution, followed by drying at 373 K for 12 h. The as-synthesized samples were calcined in static air at 873 K or 1173 K for 15 h using a heating rate of 5 K min^{-1}. Prior to some characterization studies and catalytic tests (Section 2.3), the calcined samples were pretreated in He at 623 K for 30 min and heated or cooled in the same gas to the desired reduction temperature (573 or 773 K), which was done in a mixture of 5 vol% H_2 in He during 30 min. The ramp used in the above temperature programs was 5 K min^{-1}. Along the manuscript, the sample notation makes reference to the precursor or support, i.e. HT (hydrotalcite), MA (malachite), IA (impregnated alumina), and IS (impregnated silica). The sample codes additionally incorporate the acronym 'AS' (as-synthesized) or 'C*x*–R*y*', where 'C*x*' stands for calcination at temperature *x* and 'R*y*' stands for reduction at temperature *y* (in Kelvin).

2.2. Catalyst characterization

The chemical composition of the samples was determined by X-ray fluorescence in a Philips PW 2400 spectrometer. Before analysis, the solid was mixed with $Li_2B_4O_7$ and LiI as tensoactive agent, and the mixture was fused at 1423 K in a Perle'X-3 radiofrequency furnace.

Ex situ X-ray diffraction of the as-synthesized and calcined samples was studied in a Bruker AXS D8 Advance diffractometer equipped with a Cu tube, a Ge(1 1 1) incident beam monochromator (λ = 0.1541 nm), and a Vantec-1 PSD. Data were recorded in the range of 5–70° 2θ with a step size of 0.02° and a counting time of 4 s per step.

In situ X-ray diffraction during reduction of the calcined samples was performed in a Bruker-AXS D5005 θ–θ diffractometer equipped with a Bruker-AXS MRI high-temperature chamber and a diffracted beam graphite monochromator using Cu Kα radiation. A thin layer of sample (ca. 30 mg) was mounted on the Pt_{90}–Rh_{10} heater strip by placing a few droplets of a suspension of finely ground sample in ethanol followed by drying under ambient conditions. The sample was dried in N_2 at 473 K (30 min) and reduced in a mixture of 5 vol% H_2 in N_2 at 573 K or 773 K (30 min) using a total flow of 42 cm^3 STP min^{-1}. The patterns were recorded at each temperature after N_2 flushing for 10 min. The heating rate between each temperature step was 5 K min^{-1}. Data were collected at 10–70° 2θ with a step size of 0.02° and a counting time of 1 s per step.

Thermogravimetry was performed in a Mettler Toledo TGA/SDTA851e microbalance. Analyses were performed in air (50 cm^3 STP min^{-1}), ramping the temperature from 298 to 1173 K at 5 K min^{-1}.

TEM was measured in a JEOL JEM-1011 microscope operated at 100 kV and equipped with a SIS Megaview III CCD camera. A few droplets of the sample suspended in ethanol were placed on a carbon-coated copper grid, followed by evaporation at ambient conditions.

N_2 isotherms at 77 K were measured in a Quantachrome Autosorb 1-MP analyzer. Prior to analysis, the samples were degassed in vacuum at 573 K for 12 h.

Temperature-programmed reduction with hydrogen (H_2-TPR) was measured in a Thermo TPDRO 1100 set-up equipped with a thermal conductivity detector. The sample (ca. 10 mg) was loaded in the quartz microreactor (11 mm i.d), pretreated in N_2 (20 cm^3 STP min^{-1}) at 573 K for 30 min, and cooled to 323 K in the same atmosphere. The analysis was carried out in a mixture of 5 vol% H_2 in N_2 (20 cm^3 STP min^{-1}), ramping the temperature from 323 to 1173 K at 10 K min^{-1}.

X-ray photoelectron spectroscopy (XPS) measurements were obtained using a VG-Microtech Multilab 3000 spectrometer equipped with Mg Kα ($h\nu$ = 1253.6 eV) and Al Kα ($h\nu$ = 1486.6 eV) excitation sources, a nine-channeltron detection system, and a hemispheric electron analyzer. The sample was outgassed overnight at room temperature in a UHV chamber (<5 × 10^{-8} Torr). In some cases, before XPS measurements, the specimen was transferred to a high-pressure reaction cell (10^{-3} Torr) attached to the analysis chamber of the spectrometer and pretreated in H_2 at 573 or 773 K. Reduced samples were immediately transferred to the analysis chamber. All binding energies were referenced to the C 1*s* line at 284.6 eV, and the integrated intensities were corrected by atomic sensitivity factors [24].

N_2O pulse chemisorption was carried out in the same Thermo TPDRO 1100 unit used for H_2-TPR. The sample (ca. 200 mg) was

loaded in the microreactor, pretreated in N_2 (20 cm^3 STP min^{-1}, 573 K, 30 min), reduced in a mixture of 5 vol% H_2 in N_2 (42 cm^3 STP min^{-1}, 573 or 773 K, 30 min), and flushed in He (20 cm^3 STP min^{-1}, 423 K, 30 min). Thereafter, 0.34 cm^3 of pure N_2O (loop volume) were successively pulsed over the catalyst bed every 4 min at 423 K in He (20 cm^3 STP min^{-1}). A cold trap of liquid nitrogen was used to remove unreacted N_2O from the outlet stream, so that only N_2 produced by N_2O decomposition was detected by the thermal conductivity detector. The copper surface area was calculated from the amount of N_2O decomposed using an atomic surface density of 1.46×10^{19} atoms m^{-2} [25].

2.3. Catalytic tests

The gas-phase hydrogenation of propyne was studied at ambient pressure in a MicroActivity Reference setup (PID Eng&Tech). The catalyst (150 mg, sieve fraction 200–400 μm) was loaded in the 12 mm i.d. quartz microreactor, heated in He at 573 K for 30 min, and prereduced in 5 vol% H_2 in He (42 cm^3 STP min^{-1}) as described in Section 2.1. The catalysts were tested isothermally at intervals of 50 K in the range of 423–523 K using a typical feed mixture of C_3H_4:H_2:He = 2.5:7.5:90 and a total flow of 42 cm^3 STP min^{-1} (space velocity, SV = 16,800 cm^3 h^{-1} g^{-1}). Each temperature was hold for a period of 5 h. Two aspects regarding the testing protocol were evaluated: (i) the influence of starting from the highest to the lowest temperature or *vice versa*, and (ii) the influence of using fresh catalyst at each individual temperature or using the same load for the different temperatures. The effect of the hydrogen-to-propyne ratio (H_2:C_3H_4 = 1–12) was also studied. For this purpose, the inlet C_3H_4 concentration was kept at 2.5 vol% and the H_2 concentration was decreased from 30 to 2.5 vol% by balancing the mixture with He in order to keep the total flow constant. Propyne, propene, and propane were analyzed on-line by a gas chromatograph (Agilent GC6890 N) equipped with a GS-GasPro column and a thermal conductivity detector. The selectivity to propene (propane) was determined as the amount of propene (propane) formed divided by the amount of reacted propyne. The fractional selectivity to oligomers was obtained as: S(oligomers) = 1 − S(alkene) − S(alkane). In particular tests, the gas at the reactor outlet was collected and oligomers were identified off-line by a gas chromatograph (Agilent GC6890 N) equipped with a HP-5 column and coupled to a mass selective detector with electronic impact ionization source (Agilent 5973).

2.4. Operando FTIR spectroscopy

Fourier transform infrared spectroscopy was carried out in a Nicolet 5700 spectrometer (Thermo Scientific) using a Spectratech collector II diffuse reflectance (DRIFT) accessory equipped with a high-temperature chamber, ZnSe windows, and a MCT detector. The sample cell was filled with powdered catalyst and carefully leveled off to reduce reflections off the sample surface and to ensure reproducible results. The experiments were carried out using the standard conditions described in Section 2.3. Spectra were automatically recorded every 120 s during 4 h using KBr (Aldrich, IR spectroscopy grade) under reaction conditions using the spectrum of the activated catalyst before reaction as the background. The range 650–4000 cm^{-1} was covered by co-addition of 32 scans at a nominal resolution of 4 cm^{-1}.

3. Computational details

Propyne hydrogenation on Cu and Ni was studied by means of periodic Density Functional Theory (DFT) applied to slabs with the VASP code [26]. The surfaces include clean Ni(1 1 1) and Cu(1 1 1). The calculated cell parameters were 3.551 and 3.676 Å, in close agreement with those experimentally determined 3.524 and 3.615 Å for Ni and Cu, respectively [27]. The (1 1 1) slabs consisted of four atomic layers and a $p(3 \times 3)$ reconstruction for the study of molecular adsorption and hydrogenation processes. In addition, Cu(2 1 1) with a $p(3 \times 1)$ reconstruction and nine layers was also employed to calculate molecular adsorption. In the case of oligomerization, the unit cells were $p(2 \times 4)$ thus allowing to include two propyne molecules along the long axis. This represents one of the multiple possibilities to study the process, since oligomerization can take place also from any partially hydrogenated moiety. For the (1 1 1) surfaces, the two uppermost layers were allowed to relax together with the adsorbates. The Monkhorst–Pack [28] k-point meshes were $3 \times 3 \times 1$ for $p(3 \times 3)$ and $5 \times 3 \times 1$ for $p(2 \times 4)$. The RPBE functional has been employed to obtain the energy [29], inner electrons have been replaced by PAW pseudopotentials [30], and the monoelectronic valence states have been expanded with plane waves with kinetic energies lower than 400 eV. For Ni-containing structures spin polarization was taken into account. The barriers for hydrogenation steps, which follow a Horiuti–Polanyi mechanism [31], and oligomerization were obtained through the Climbing Image version of the Nudged Elastic Band (CI-NEB) method [32].

Ab initio thermodynamics were employed to determine the formation of hydrides that are known to have a crucial role in the selectivity of the process [33]. The unit cell employed was a $p(2 \times 2)$ and H atoms were initially place on all four fcc positions of the lattice and similarly H atoms were introduced in deeper surface layer following the procedure proposed by Greeley et al. [34]. In that case sampling was set to $5 \times 5 \times 1$ k-points. The Gibbs energy was approximated as $\Delta G \approx E_{\mathrm{slab}+n\mathrm{H}} - E_{\mathrm{slab}} - (n/2)\mu(\mathrm{H}_2)$, where $E_{\mathrm{slab}+n\mathrm{H}}$ is the energy of the slab containing nH atoms, E_{slab} is the energy of the slab, and $\mu(H_2)$ is the chemical potential of hydrogen [35].

Additional calculations were performed to analyze the solubility and segregation of aluminum in the copper and nickel oxides. The corresponding descriptions are included as footnotes due to their specific characteristics.

4. Results and discussion

4.1. Catalyst characterization

4.1.1. As-synthesized samples

Fig. 1a shows the X-ray diffraction patterns on the as-synthesized samples. The material prepared by precipitation of Cu^{2+} with NaOH + Na_2CO_3 (MA-AS) shows characteristic reflections of malachite. Coprecipitation of a cationic solution containing Cu^{2+} and Al^{3+} (Cu/Al = 3) with the same precipitating agents led to HT-AS. The Cu/Al ratio measured by XRF was 3.3. The sample exhibited the pattern of the layered Cu–Al hydrotalcite as the main crystalline phase, with the characteristic basal (0 0 l) reflections at low diffraction angles [36,37]. According to the card JCPDS 46-0099, which closely matched our pattern (Fig. S1), this hydrotalcite has monoclinic structure. The reflections at 44.5° and 48° 2θ were not collected in the original card but the latter have also been identified and assigned to the hydrotalcite phase by Segal et al. [37]. The c' parameter of the sample (0.7537 nm), corresponding to the thickness of one brucite-like layer and one interlayer [36], was determined from the (0 0 3) reflection at 11.7° 2θ. In agreement with other works involving the synthesis of Cu–Al hydrotalcite [37–40], trace amounts of malachite were observed in HT-AS. The presence of this secondary phase has been related to the Jahn–Teller distortion of copper in octahedral coordination. We also conducted the coprecipitation of copper and aluminum solutions at

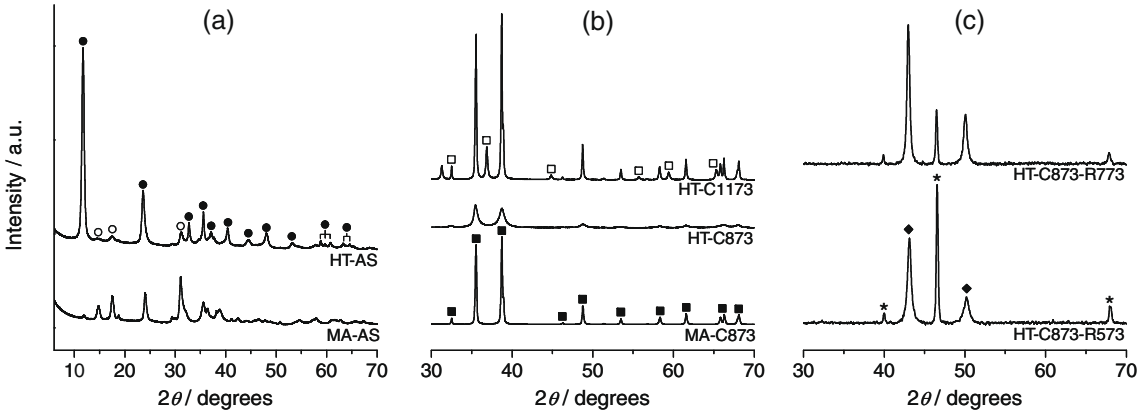

Fig. 1. XRD patterns of the as-synthesized Cu–Al hydrotalcite and malachite (a) and the products of calcination (b) and reduction (c). Crystalline phases: (●) hydrotalcite (JCPDS 46-0099), (○) malachite (JCPDS 75-1163), (■) CuO (JCPDS 48-1548), (□) $CuAl_2O_4$ (JCPDS 78-1605), and (♦) Cu (JCPDS 86-1326). Reflections marked by the asterisk belong to the Pt_{90}-Rh_{10} heater strip of the cell where the samples were mounted for *in situ* reduction.

Cu/Al ratios of 1 and 2. The latter two samples evidenced no sign of hydrotalcite, i.e. malachite was the only crystalline phase detected (Fig. S2). These samples were not considered for further characterization and catalytic tests. HT-AS and MA-AS are representative of the hydrotalcite and malachite precursors, respectively. Transmission electron microscopy (Fig. 2) shows that MA-AS consisted of spherical-like particles in the range of 30–60 nm, while the hydrotalcite sample displays the characteristic platelets [41] with an average length of 130 nm and a thickness of 20 nm. The particle morphology of MA-AS was not identified in HT-AS, further supporting the minor presence of the malachite phase in the hydrotalcite sample. The total BET surface area of MA-AS and HT-AS, determined from N_2 adsorption, was 42 and 65 $m^2\,g^{-1}$, respectively.

The thermogravimetric profiles of MA-AS and HT-AS in air are shown in Fig. 3. Malachite decomposed in one step with simultaneous production of H_2O and CO_2. The transition temperature was 585 K (inset) and the total weight loss was 24%. In contrast, HT-AS exhibited a three-step decomposition pattern with a total weight loss of 32%. The first two steps are characteristic of hydrotalcite-like compounds [36]. Step I (transition temperature = 400 K, weight loss = 10%) corresponds to interlayer water removal. This was followed by step II (weight loss 17%), comprising the removal of interlayer carbonate and the dehydroxylation of the brucite-like sheets. Step II occurred in the broad temperature range of 400–650 K, rendering no defined transition temperature in the derivative curve. Step III (transition temperature = 845 K, weight loss = 5%) has been particularly observed in copper-containing hydrotalcites and corresponds to the decomposition of stable residual carbonates [37–39]. Accordingly, total decomposition of HT-AS requires 873 K, which was adopted as the standard calcination temperature of all catalyst precursors in this study. The amount of the malachite phase in HT-AS estimated from thermogravimetry was <10%.

4.1.2. Calcined samples

As shown in Fig. 1b, calcination of MA-AS and HT-AS at 873 K led to CuO (tenorite), while both tenorite and $CuAl_2O_4$ spinel coexisted in the hydrotalcite-derived oxide calcined at 1173 K. No reflections associated with any crystalline form of alumina were detected. The CuO reflections in the XRD patterns of HT-C873 and HT-C1173 were exactly at the same position as in pure copper oxide, indicating that the Cu–Al oxide does not form a solid solution. In contrast, the NiO reflections in calcined Ni–Al hydrotalcite were shifted to higher diffraction angles compared due to the substitution of Al^{3+} in the nickel oxide lattice [16]. DFT calculations [42] support this observation. The solubility of Al in the position of Cu or Ni in their corresponding oxygen lattices (NiO or CuO) is more energetically favored in NiO than in CuO by ca. 1 eV. The CuO reflections in the XRD pattern of HT-C873 were much less intense and broader than in MA-C873, indicating higher crystallinity of the latter sample. The average crystallite size of CuO, determined from the (1 1 1) reflection at 38.7° 2θ, was 11 nm for HT-C873 and 50 nm for MA-C873. Similarly, the intensity and sharpness of the XRD reflections in the hydrotalcite calcined at 1173 K were markedly larger when compared to calcination at 873 K. The average crystallite sizes of CuO and $CuAl_2O_4$ in HT-C1173 were estimated at 52 and 35 nm, respectively. In line with XRD, TEM confirmed the high degree of sintering of the malachite-derived CuO as well as of the high-temperature calcined hydrotalcite (compare MA-C873 and HT-C1173 with HT-C873 in Fig. 2). N_2 adsorption concluded that the total surface area of HT-C873 (S_{BET} = 71 $m^2\,g^{-1}$) drastically decreased in MA-C873 (S_{BET} = 4 $m^2\,g^{-1}$) and HT-C1173 (S_{BET} = 15 $m^2\,g^{-1}$). The characterization results evidence the superior features of the hydrotalcite route in attaining well-dispersed mixed oxides with high metal loadings, particularly in the specimen calcined at 873 K. It should be mentioned that the calcined hydrotalcites contained 65 wt% Cu and 8 wt% Al while calcined malachite contained 80 wt% Cu.

4.1.3. Reduced samples

H_2-TPR was used to investigate the reducibility of the copper oxides derived from different precursors and calcination temperatures (Fig. 4). The profile of HT-C873 shows a main peak of hydrogen consumption at 560 K attributed to the reduction of bulk CuO [43] with a shoulder at 515 K due to the reduction of highly-dispersed CuO particles [44]. Both features were shifted to slightly higher temperature in HT-C1173 probably due to the occurrence of larger CuO crystals. Besides, the latter sample exhibited a shoulder at 600 K and a broad low-intensity peak at 720 K. Dumas et al. [43] assigned the feature at 600 K to the two-step reduction of relatively large copper oxide particles: $CuO \rightarrow Cu_2O$ (580 K) and $Cu_2O \rightarrow Cu$ (around 600 K). The hydrogen consumption at 720 K is attributed to copper reduction in $CuAl_2O_4$ [43]. Peak integration enabled to estimate that the spinel comprises 10% of copper in HT-C1173, the rest being tenorite. Attending to the stoichiometry of the spinel and chemical composition analysis, it can be concluded that ca. 75% of the total aluminum in the solid took part in $CuAl_2O_4$, while the remaining 25% was in the form of amorphous alumina. The main reduction peak of MA-C873 occurred at 560 K, i.e. very similar temperature to that in HT-C873. In contrast, the malachite-derived CuO had no shoulder <525 K

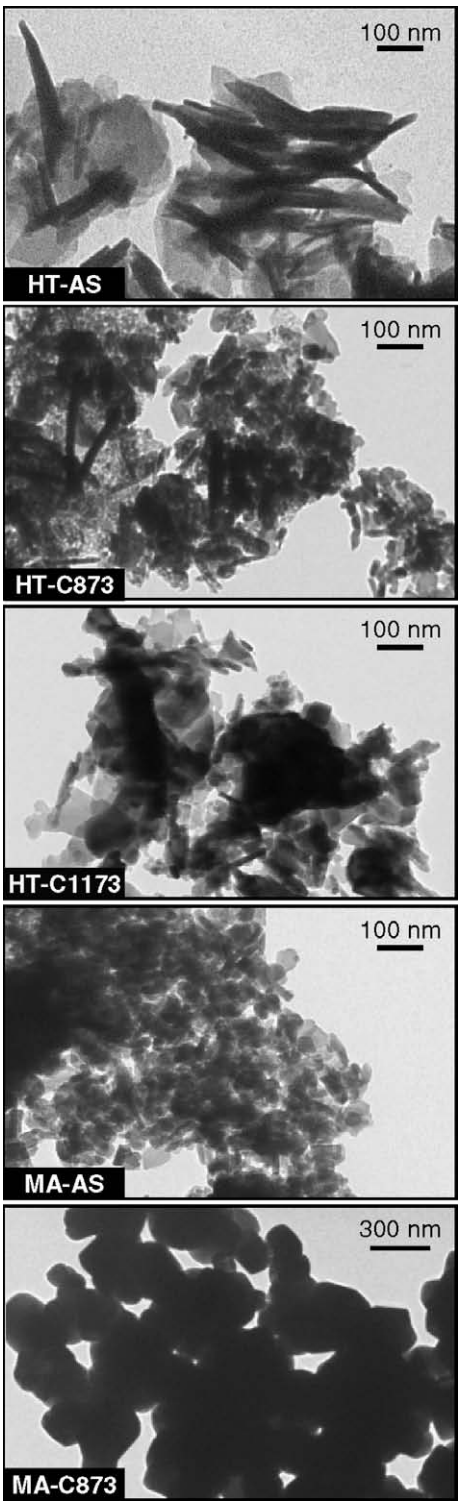

Fig. 2. TEM micrographs of Cu-Al hydrotalcite and malachite and calcined products.

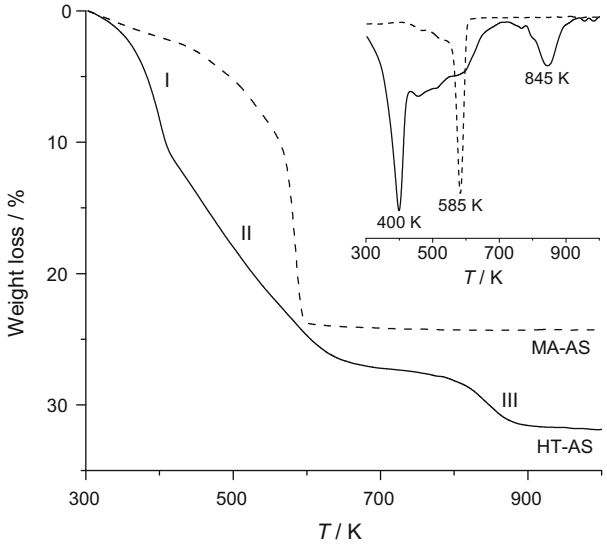

Fig. 3. TGA profiles of the as-synthesized Cu–Al hydrotalcite and malachite in air and derivative of the weight loss (inset).

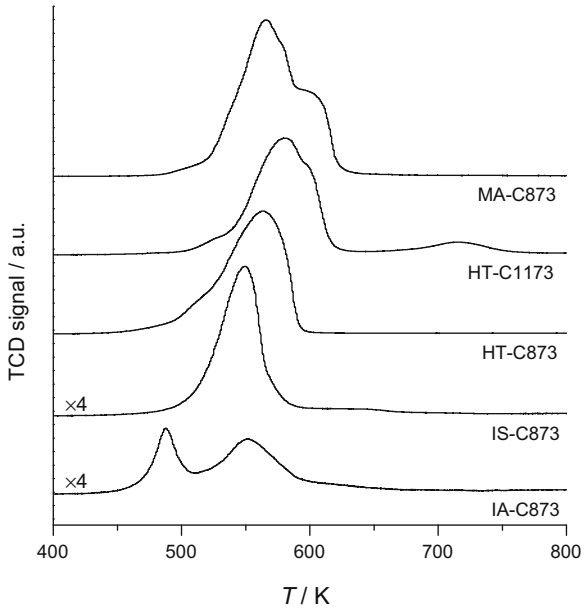

Fig. 4. H_2-TPR profiles of the oxides derived from calcination of Cu–Al hydrotalcite and malachite and the supported copper catalysts.

and displayed a shoulder around 600 K due to the presence of large CuO particles. This agrees with XRD and TEM analyses. The very similar reduction temperature of MA-C873 (pure CuO) and HT-C873 (Cu–Al oxide) further confirmed that copper and aluminum do not form a solid solution in the calcined hydrotalcite. In contrast, Ni^{2+} reduction in calcined Ni–Al hydrotalcite (925 K) was shifted to a much higher temperature than in pure nickel oxide (675 K) [16]. The dissolution of aluminum in the nickel oxide lattice, forming a $NiAlO_x$ solid solution, makes Ni^{2+} more resistant against reduction. The reduction of the spinel also occurred at a much lower temperature for $CuAl_2O_4$ (720 K) than for $NiAl_2O_4$ (1050 K). The H_2-TPR profiles of the supported CuO/Al_2O_3 (IM-C873) and CuO/SiO_2 (IS-C873) catalysts are also shown in Fig. 4. Attending to previous results [43–45], the peak at 490 K in the alumina-supported catalyst is assigned to the reduction of the highly-dispersed oxidic copper species, which can include isolated copper ions and small two- and three-dimensional clusters. The peak at 560 K was ascribed to the reduction of bulk-like CuO phases. When silica was used as the support, only the latter feature was evidenced.

H_2-TPR and XRD were also carried out over *in situ* reduced samples mimicking the pretreatment prior to catalytic tests (5 vol% H_2 in He, 573 or 773 K, 30 min). The samples prereduced under these

conditions showed no hydrogen consumption due to full reduction to metallic copper. In agreement, the diffraction patterns only revealed reflections of metallic copper (Fig. 1c). The average Cu crystallite size, estimated by application of the Scherrer method in the (1 1 1) reflection at 43° 2θ, moderately increased upon increasing the reduction temperature: 15 nm in HT-C873-R573 and 20 nm in HT-C873-R773. The total surface area of the reduced samples was very similar to the values in the corresponding oxide precursors (Table 1), also suggesting minor sintering upon reduction.

4.1.4. Surface composition and copper dispersion

X-ray photoelectron spectroscopy analyses of representative hydrotalcite-derived samples were carried out in order to gain insights into the chemical state of surface copper and the metal distribution within the catalyst particle (Fig. 5). The calcined hydrotalcite HT-C873 showed photoelectron lines at 933.8 eV (Cu $2p_{3/2}$) and 76.2 eV (Cu $3p_{3/2}$), characteristic of Cu^{2+} ions in copper(II) oxide [46]. The broad line at 942.8 eV belongs to the shake-up satellite of Cu^{2+} [47]. The core level of Al 2*p*, represented by the line around 74 eV, is typical of Al_2O_3 [48]. This feature was essentially constant irrespective of sample pretreatment. Calcination at 1173 K did not involve changes in the position of the copper-related lines. No line at 935 eV, characteristic of $CuAl_2O_4$ [49], was detected in HT-C1173. This suggests that the crystalline spinel phase observed by X-ray diffraction was not at the catalyst surface. As shown in Table 1, the Cu/Al ratio of HT-C873 and HT-C1173 determined by XPS (0.32 and 0.18, respectively) was much lower than the bulk Cu/Al ratio of 3.3 determined by XRF. Consequently, the surface of the oxide is enriched by aluminum, particularly at higher calcination temperature. Bolt et al. [50] also reported the notable penetration of copper ions into alpha and gamma alumina at 773 K and particularly at 1173 K, rendering an Al-rich surface. The segregation of copper in calcined Cu–Al hydrotalcite was significantly more pronounced than that of nickel in calcined Ni–Al hydrotalcite [16]. The XPS-determined Ni/Al ratio in Ni–Al hydrotalcite calcined at 773 K was 1.4, while the Cu/Al ratio in Cu–Al hydrotalcite calcined at 873 K was 0.32. The faster and deeper segregation of copper with respect to nickel has been explained by the fact that the diffusion into the bulk occurs through the formation of the spinel form of the metal and copper spinel has a higher rate of formation than the nickel spinel [50].

The XPS spectra of the reduced samples show the shift of the Cu $2p_{3/2}$ core level from 933.8 to 932 eV and the shift of the Cu $3p_{3/2}$ core level from 76.2 to 75 eV. The new lines are characteristic of Cu^0 [51]. Further evidence of the copper reduction stems from the disappearance of the shake-up satellite of Cu^{2+}. The origin of the satellite peak is considered to be the promotion of 3*d* electrons to 4*s* and/or 4*p* levels or, alternatively, a charge transfer of bonding electrons to unfilled 3*d*. This transfer cannot occur in Cu^+ and Cu^0 because of their completely filled 3*d* shells. One can argue that HT-C873-R773 still contains a minor fraction of surface Cu^{2+}. This statement arises from the fact that: (i) the satellite is still vaguely visible, and (ii) the position of the Cu $2p_{3/2}$ and Cu $3p_{3/2}$ core levels (932.7 and 75.6 eV, respectively) is intermediate between the values of CuO and Cu. However, no hydrogen consumption was monitored in H_2-TPR of HT-C873-R573. Reduction of calcined Cu–Al hydrotalcites further decreased the surface Cu/Al ratio (Table 1). The extreme case is HT-C1173-R773, containing 12 atoms of aluminum per each copper atom. This is in line with the segregation energies calculated by DFT. The differential segregation energy for Al cations in CuO and Cu resulted ca. −0.35 eV more favorable in the metal [52]. The more pronounced surface Al enrichment upon reduction was also observed with Ni–Al hydrotalcite system [16].

The dissociative chemisorption of N_2O was used to determine the copper metal area (S_{Cu}) in the reduced samples (Table 2). The hydrotalcite-derived HT-C873-R573 sample exhibited the highest value of exposed Cu area, with 10.5 m^2 per gram. An increase in calcination or reduction temperature drastically decreases the copper dispersion, which is due to the attainment of larger copper crystals and the higher surface enrichment by aluminum. For example, going from HT-C873-R573 to HT-C1173-R773 implies a ten-fold decrease in S_{Cu}. These samples are highly comparable, since they come from the same precursor and therefore the bulk copper content is exactly the same. As expected, the malachite-derived sample renders a poorly dispersed catalyst, with 0.5 m^2 Cu per gram. Regarding the supported copper catalysts, silica yielded a higher exposed copper surface than alumina. In these two catalysts, the same impregnation method for copper incorporation and loading (15 wt%) were applied.

Table 1
Characterization data of the Cu-Al hydrotalcite-derived catalysts.

Sample	Phases[a]	S_{BET}[b] ($m^2\ g^{-1}$)	Molar Cu/Al ratio (–)	
			Bulk[c]	Surface[d]
HT-C873	CuO	71	3.3	0.32
HT-C873-R573	Cu	73	3.3	0.25
HT-C873-R773	Cu	68	3.3	0.19
HT-C1173	CuO + $CuAl_2O_4$	15	3.3	0.18
HT-C1173-R773	Cu	17	3.3	0.12

[a] X-ray diffraction.
[b] BET method.
[c] X-ray fluorescence.
[d] X-ray photoelectron spectroscopy.

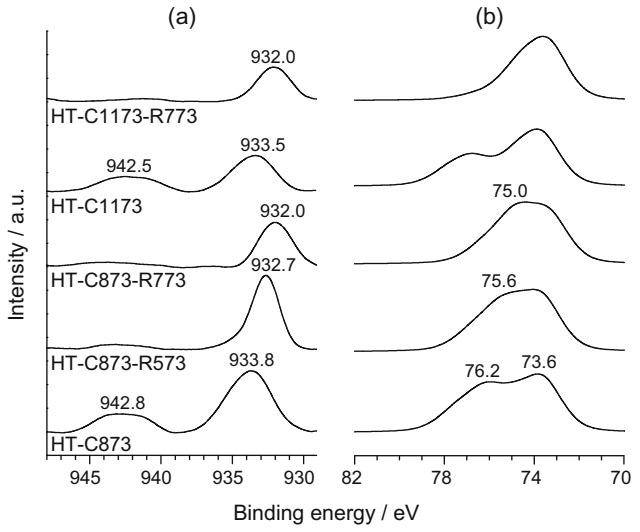

Fig. 5. Cu 2*p* (a), Cu 3*p* (b), and Al 2*p* (b) core level spectra in the calcined and reduced samples obtained from Cu–Al hydrotalcite.

Table 2
Copper metal area in reduced catalysts determined by pulse N_2O chemisorption.

Sample	S_{Cu} ($m^2\ g^{-1}$)
HT-C873-R573	10.5
HT-C873-R773	5.7
HT-C1173-R773	1.7
MA-C873-R773	0.5
IA-C873-R773	1.5
IS-C873-R773	2.6

4.2. Hydrogenation performance

4.2.1. Testing protocol

A point to first consider regards the choice of the protocol to evaluate the hydrogenation performance of copper-based catalysts. Little attention has been devoted to this aspect, which might be important to properly compare samples. Previous tests over Au/CeO_2 [14] and activated Ni–Al hydrotalcites [16] were typically conducted from the highest (573 K) to the lowest (373 K) temperature at intervals of 50 K using a H_2:C_3H_4 ratio of 3 and the same catalyst load. Following this procedure over a particular activated Cu-based hydrotalcite (HT-C873-R773), it can be observed that the propyne conversion was complete at 523 K and 473 K, while deactivation was monitored at 423 K (Fig. 6a). Propene selectivity decreased with temperature, from 75% at 523 K to ca. 30% at 423 K (Fig. 6b). Despite the gradual decrease in C_3H_4 conversion at 423 K, the selectivity to C_3H_6 remained constant. Alternative protocols involved: (i) the use of fresh catalyst at each temperature, and (ii) starting the test at the lowest temperature using the same load. Experiments using a fresh catalyst load at each temperature yielded very similar results compared to the use of the same catalyst load at the three temperatures (Fig. S3). Likewise, the C_3H_6 selectivity vs. T in up- and down-temperature cycles was practically identical (Fig. S4). Accordingly, the testing procedure is not critical for the assessment of Cu-based catalysts in partial hydrogenation. It should be stressed that in the above experiments, oligomers were the only reaction product in addition to propene, i.e. no propane was observed.

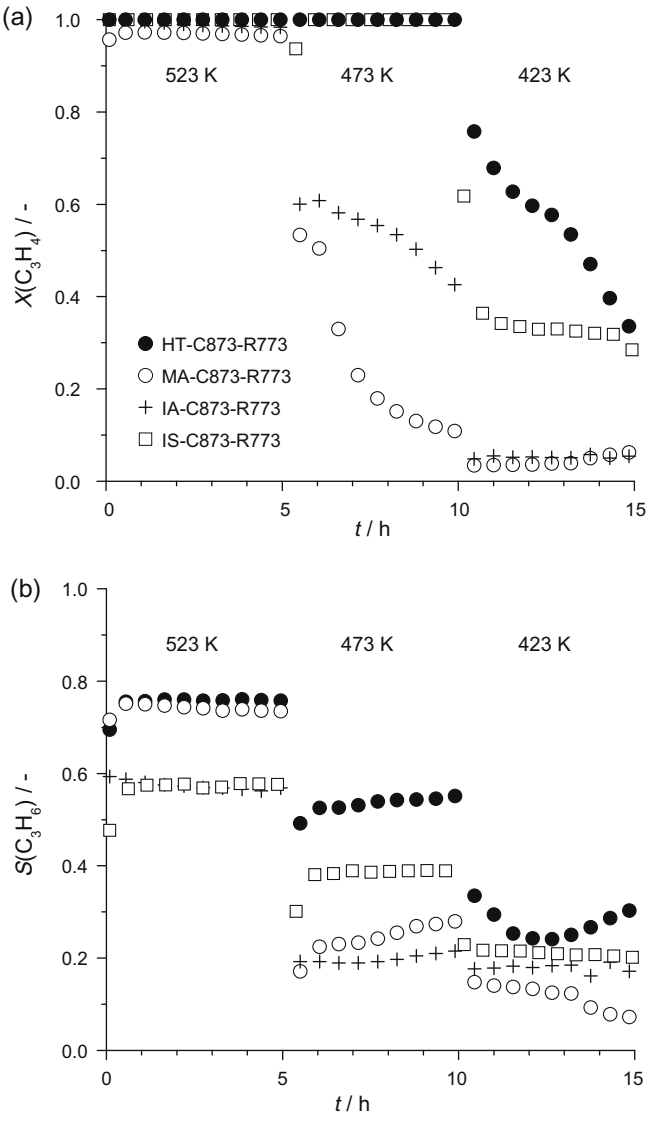

Fig. 6. Propyne conversion (a) and propene selectivity (b) vs. time during propyne hydrogenation over different Cu-based catalysts. Conditions: C_3H_4:H_2:He = 2.5:7.5:90, T = 423–523 K, SV = 16,800 cm^3 g^{-1} h^{-1}, and P = 1 bar.

4.2.2. Comparison of copper-based catalysts

The hydrogenation performance of copper-based catalysts obtained from different precursors, i.e. hydrotalcite, malachite, and supported systems, calcined and reduced at equal conditions, is compared in Fig. 6. Tests were run adopting our standard protocol, i.e. from 523 to 423 K every 50 K. Clear differences in propyne conversion and propene selectivity were observed. The hydrotalcite-derived sample (HT-C873-R773) was the most active and selective catalyst, followed by Cu/SiO_2 (IS-C873-R773). The malachite-derived (MA-C873-R773) and Cu/Al_2O_3 (IA-C873-R773) catalysts displayed much lower activity and alkene selectivity. The drop in C_3H_4 conversion at 473 or 423 K caused no change in C_3H_6 selectivity during 5 h at each temperature. For all catalysts: (i) propene selectivity decreased with the reduction in reaction temperature, and (ii) the fully hydrogenated product (C_3H_8) was not formed. The C_3H_6 selectivity dependence on temperature and product distribution (absence of alkane) agree with seminal work on supported copper catalysts by Wehrli et al. [18,19]. These common features are related to the poor hydrogenating ability of copper as a consequence of the inefficient dissociation of H_2. Mechanistic details are elaborated in Section 4.3.

Previous studies have reported fast deactivation of Cu-based catalysts in alkyne hydrogenation below 433 K, due to the build-up of oligomeric material on the catalyst surface [18–21]. According to these authors, deactivation can be minimized by applying elevated temperatures, increasing hydrogen partial pressures, using basic or neutral supports such as SiO_2 or MgO, or increasing the copper dispersion. In fact, our activated Cu–Al hydrotalcites were remarkably stable at 473 K and 523 K, as confirmed in 40-h tests (Fig. S5). Deactivation is problematic only at low-temperature ($\leqslant$423 K), where the selectivity to oligomers is as high as 80–90%. Insights into catalyst deactivation were obtained by *operando* infrared spectroscopy. Fig. 7a shows the evolution of the CH stretching region during propyne hydrogenation over HT-C873-R773 at 473 K and 423 K, with intermediate N_2 flushing steps. At both temperatures, the progressive growth of a carbonaceous layer on the catalyst surface can be observed. The bands at 2960 and 2925 cm^{-1} have been assigned to the asymmetric CH stretching of CH_3 and CH_2 groups, respectively, and the band at 2870 cm^{-1} to the symmetric CH stretching of CH_3 group [53,54]. These peaks were related to a straight chain hydrocarbon of high molecular weight [20]. The main spectral difference between the two temperatures was the more prominent presence of bands at 3015 cm^{-1} and 3085 cm^{-1} at 423 K. This can be seen more clearly in Fig. 7b, where the spectra after 4 h of experiment at each temperature starting from fresh sample are collected. These features, which are assigned to alkene C–H stretching of CH_2 groups (–CH=CH_2) [54], are regarded as crucial to explain the low-temperature deactivation behavior. These deposits block active sites and are responsible for the drop in catalytic activity. Ossipoff and Cant [20] neither observed nor discussed the bands at 3015 and 3085 cm^{-1} during *in situ* infrared spectroscopic measurements over ion-exchanged copper on silica catalyst at 433 K (at which deactivation was observed). The higher population of alkene-like compounds on the surface at 423 K was also confirmed in the low-wavenumber region (Fig. 7c). The spectra show to the typical C–H deformations bands in alkanes (1445 and 1375 cm^{-1}) [54]. The bands at 1600–1650 cm^{-1} due to C=C stretching are more intense at

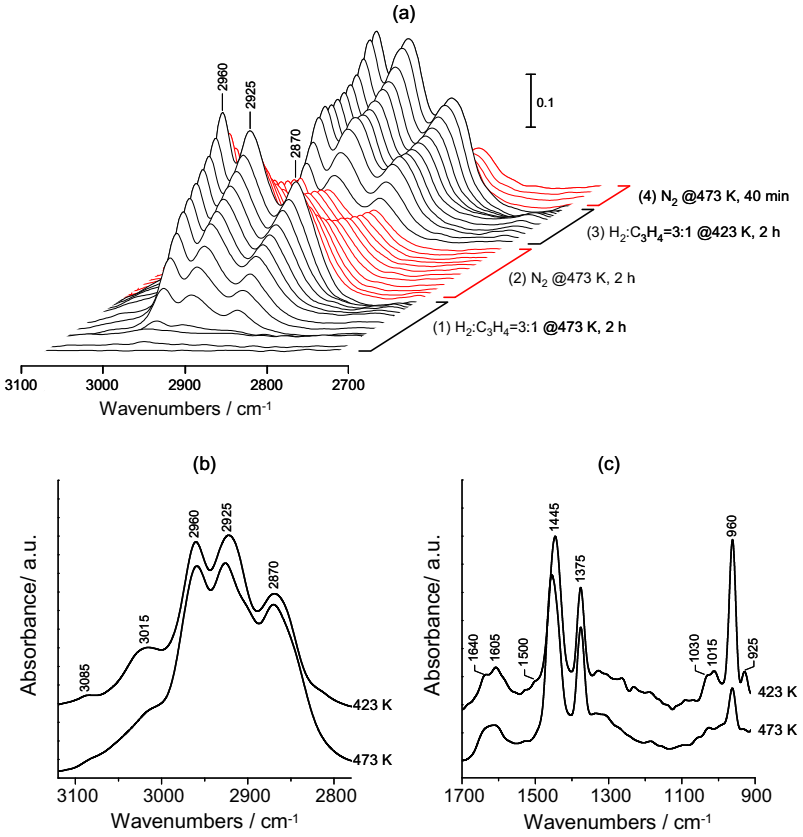

Fig. 7. (a) *Operando* DRIFTS in the CH stretching region during propyne hydrogenation over HT-C873-R773 at 473 K (1), followed by N_2 flushing at 473 K (2), again reaction at 423 K (3), and finally N_2 flushing at 473 K (4). The displayed spectra were taken approximately every 10 min; (b) and (c) show spectra after 4 h on stream at 473 or 423 K. Other conditions were as in caption of Fig. 6.

423 K, as well as absorptions due to C–H vibrations in vinyl-type (–CH=CH_2): 1015–1030, 960, and 925 cm^{-1}. As shown in Fig. 7a, when the used catalysts were exposed to N_2 for 2 h, the intensity of the bands decreased to a significant degree due to desorption of loosely bound species. However, other stable species remained on the catalyst.

Off-line GC/MS analysis of the gas at the reactor outlet over HT-C873-R773 mostly identified C6 and C9 aliphatic compounds with single or conjugated double bonds when the reaction was conducted at 473 K. At 423 K, the C6 and C9 compounds contain conjugated double bonds (–C=C–C=C–) and conjugated double and triple bonds (–C=C–C≡C–), while monoolefins were not clearly detected. The more unsaturated character of oligomers at lower temperature can be related to the faster deactivation of the copper catalyst. It should be pointed out that the GC/MS analysis was not conducted for quantitative purposes, rather to identify the type of higher hydrocarbon produced in the reaction. Fig. S6 shows typical chromatograms and some of the compounds related to the corresponding masses.

The hydrotalcite-derived catalyst, being the most efficient one from the comparison in Fig. 6, was further optimized by variation of the activation conditions, i.e. the calcination and reduction temperatures (Fig. 8). The activity and selectivity trends explained above apply here too. The best catalyst was HT-C873-R573, showing stable C_3H_6 selectivity slightly over 80%. In comparison with other samples, this particular catalyst was highly resistant to deactivation, as evidenced by the full degree of C_3H_4 conversion at 423 K. Calcination and/or reduction of the Cu–Al hydrotalcite at higher temperature, represented by HT-C1173-R773 and HT-C873-R773, respectively, rendered less active and selective catalysts.

Fig. 9 shows the correlation between the hydrogenation performance at 473 K and the copper metal area of the reduced catalysts determined by N_2O pulse chemisorption. The reaction rate (open symbols) increased abruptly with the copper dispersion and remains constant at $S_{Cu} > 2\ m^2\ g^{-1}$. The C_3H_6 selectivity (solid symbols) increased gradually with the exposed copper surface. Obviously, the opposite trend is attained with the selectivity to oligomers, as no propane was observed. Data points belonging to the hydrotalcite-derived samples are highly comparable, since they all come from the same precursor. The result in Fig. 9 agrees previous conclusions by Trimm et al. [18,19], who concluded that the copper dispersion was the key factor to design efficient Cu-based catalysts for partial alkyne hydrogenation. In quantitative terms, we have demonstrated that the hydrotalcite route maximizes the exposed copper surface area due to the high: (i) metal loading, (ii) metal interdispersion, and (iii) specific surface area imposed by this layered precursor. The optimally activated hydrotalcite exceeds the performance of Cu/SiO_2, which has been the preferred supported system in earlier studies [19]. Despite being the most efficient copper catalyst, activated Cu–Al hydrotalcites have significant room for improvement. This is due to the surface segregation of aluminum, which reduces the potential of increasing the concentration of exposed copper. Therefore, our further steps in designing more efficient copper catalysts will focus on modifying the composition of the starting hydrotalcite, particularly replacing Al^{3+} by other transition metal, in order to maximize the amount of copper on the catalyst surface.

4.2.3. Copper vs. nickel

The hydrogenation performance of activated Cu–Al and Ni–Al hydrotalcites has been compared with respect to temperature

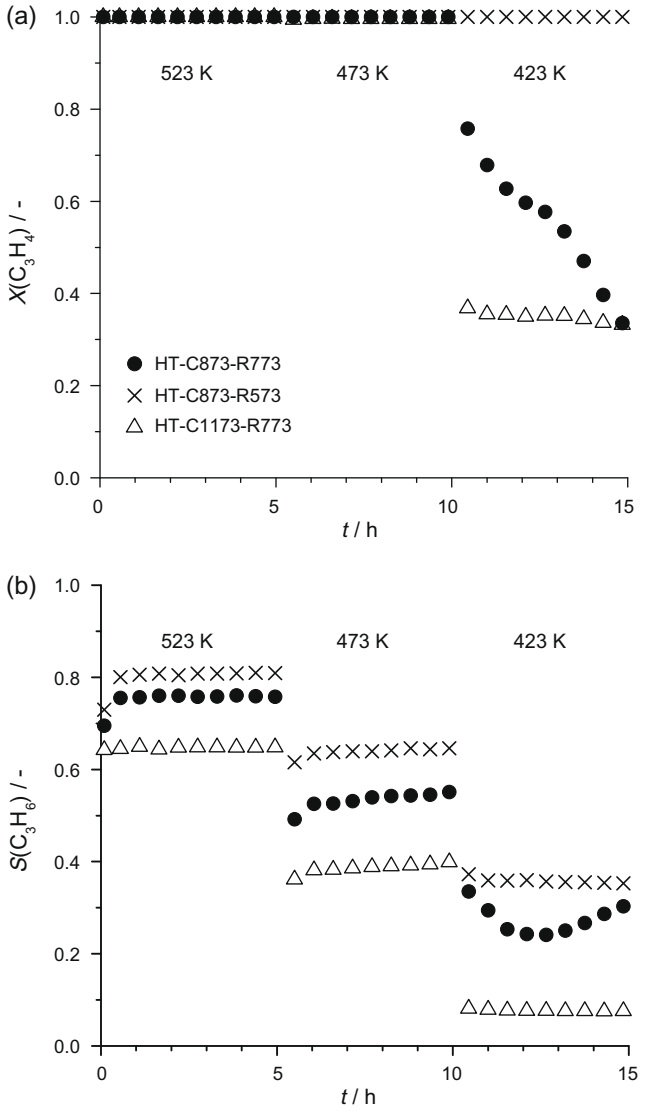

Fig. 8. Influence of the activation conditions of the Cu–Al hydrotalcite on the propyne conversion (a) and propene selectivity (b). Conditions were as in caption of Fig. 6.

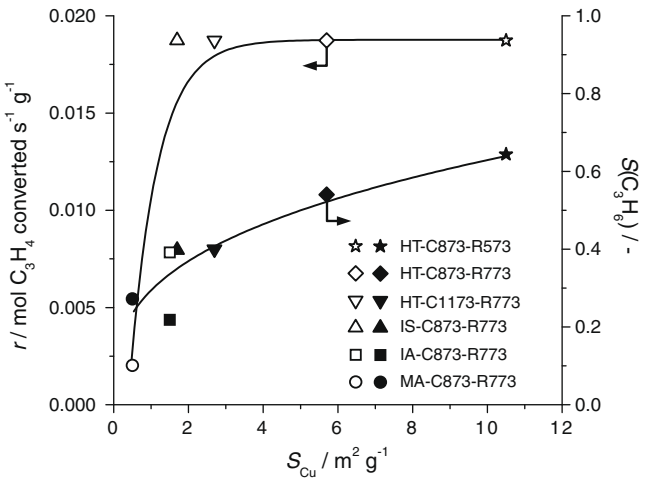

Fig. 9. Dependence of the reaction rate (open symbols) and propene selectivity (solid symbols) at $T = 473$ K on the specific surface area of copper in the catalysts. Other conditions were as in the caption of Fig. 6.

and hydrogen-to-propyne ratio. This enables a better understanding of the behavior of both metals in alkyne hydrogenation and opens the way for mechanistic studies using DFT. In the comparison, HT-C873-R773 was taken as the copper catalyst; the nickel one, named 'C773-R773', was the best catalyst identified in [16]. The reader is referred to our previous publication for detailed characterization of this sample. Although HT-C873-R573 was somewhat more efficient than HT-C873-R773, the conclusions of the comparison are invariable as the studied dependences (T, H_2:C_3H_4 ratio) did not qualitatively change with the activation (calcination and/or reduction) conditions.

The dependence of propyne conversion and selectivity to products on temperature (Fig. 10) reveal a number of distinct features between both metals:

(i) Nickel requires an activation period of ca. 5h at 523 K, in which the C_3H_6 selectivity progressively increases from 0% to 75% (Fig. 10b) and the C_3H_8 selectivity experiences a concomitant decrease (Fig. 10c). Contrarily, copper shows no activating period; the C_3H_6 selectivity is practically constant at 75% since the beginning of the experiment. The build-up of carbon-containing species in the Ni catalyst (sub-)surface is responsible for the remarkable increase in C_3H_6 selectivity in early stages of the reaction [16]. Palladium experiences the same activation [2]. Teschner et al. [11] have shown that dissolution of carbon (derived from fragmentation of alkyne molecules) in interstitial sites of Pd generates metastable subsurface palladium carbides that turn hydrogenation more selective. For Pd and Ni, the population of (sub-)surface sites, i.e. carbide and hydride formation, governs the hydrogenation steps on the surface, which is not the case for Cu.

(ii) Propene selectivity strongly decreases with a decrease in temperature over copper. In contrast, the $S(C_3H_6)$ over nickel is much less sensitive to temperature changes (Fig. 10b).

(iii) No propane was observed on copper, while the $S(C_3H_8)$ over nickel amounts to 10–20% (Fig. 10c).

(iv) Oligomerization is way more extensive on copper than on nickel. At low-temperatures, the selectivity to oligomers amounted to ca. 80% on Cu, while Ni shows ca. 15% (Fig. 10d).

(v) As seen by the degree of propyne conversion in Fig. 10a, Cu was more active than Ni at 523 and 473 K. At 423 K, the copper catalyst deactivates due to extensive oligomerization.

(vi) The nature of the oligomers over Cu and Ni at 473 K is markedly different. Copper mainly formed aliphatic C6 and C9 compounds with single or conjugated double bonds. Nickel formed C4–C8 in addition to C6 and C9, the molecules contain more hydrogen, and aromatic compounds also appeared (Fig. S6). The more complex oligomer composition over nickel reveals the activity of nickel steps to crack C–C bonds [55] and the high potential for hydrogenation.

The effect of the feed hydrogen-to-propyne ratio on the alkyne conversion and the selectivity to products is plotted in Fig. 11. Data points of activated Ni–Al hydrotalcite were gathered at 523 K [16], while 473 K was selected for the activated Cu–Al hydrotalcite. The product distribution over Cu is not strongly affected by the inlet partial H_2 pressure. The selectivity to propene at very low H_2:C_3H_4 ratios (1) is relatively low (30%) in favor of a higher selectivity to oligomers (70%). In the other extreme, i.e. at very high H_2:C_3H_4 ratios (12), the selectivity to propene was 35% at the expense of propane. However, it is remarkable that even with this hydrogen excess, the selectivity to the alkane is just 10%. In the broad range of H_2:C_3H_4 ratios from 2 to 10, the $S(C_3H_6)$ is within the narrow range of 45–50%, the S(oligomers) is within 50–55%,

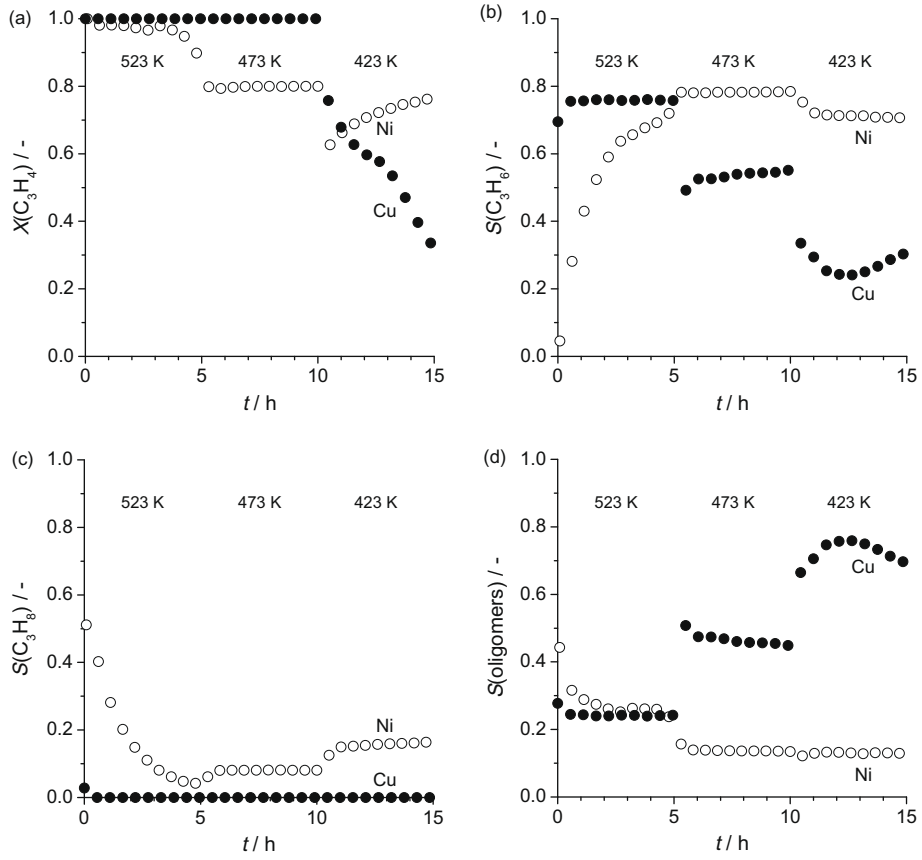

Fig. 10. Comparison of copper (●) and nickel (○) catalysts derived from hydrotalcite precursors for propyne hydrogenation. The Cu catalyst was HT-C873-R773 and the Ni catalyst was reported elsewhere with code C773-R773 [16]. Conditions were as in caption of Fig. 6.

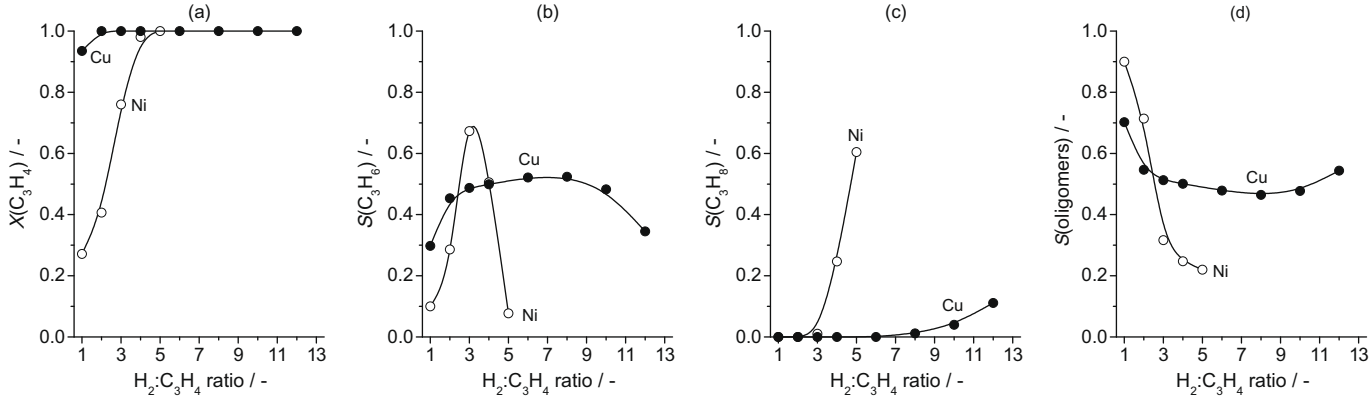

Fig. 11. Conversion of C_3H_4 (a) and selectivity to C_3H_6 (b), C_3H_8 (c), and oligomers (d) vs. the H_2:C_3H_4 ratio over copper (●) and nickel (○) catalysts. The Cu catalyst was HT-C873-R773 and the Ni catalyst was reported elsewhere with code C773-R773 [16]. Conditions: T = 473 K (Cu) or 523 K (Ni), SV = 16,800 $cm^3\ g^{-1}\ h^{-1}$, and P = 1 bar.

and the $S(C_3H_8)$ is virtually zero. Propyne conversion was practically complete at any ratio. A different picture arises over nickel, which is markedly more dependent on the partial H_2 pressure in the feed. First of all, the propyne conversion was much lower than on copper at H_2:C_3H_4 = 3. The dependence of $S(C_3H_6)$ on the H_2:C_3H_4 ratio presents a steep volcano plot, with an optimal value of ca. 70% at H_2:C_3H_4 = 3 and values as low as 10% at H_2:C_3H_4 of 1 and 5. This can be explained attending to the production of green oil and the fully hydrogenated alkane. The selectivity to oligomers is > 70% at H_2:C_3H_4 < 3, while the selectivity to propane steeply increases at H_2:C_3H_4 > 3. The almost no dependence of the C_3H_6 on the partial H_2 pressure over copper is advantageous for practical purposes, as it enables easier operation when the alkyne concentration in the feed changes due to the operation of the steam cracker (different raw material). However, in the case of nickel, a very precise control of the feed H_2:C_3H ratio is required to obtain high propene selectivity.

4.3. Density Functional Theory

Several of the above observations, in particular the comparison between Cu and Ni catalysts in alkyne hydrogenation, can be rationalized by means of DFT simulations. We have analyzed the individual adsorption of C_3H_4 and C_3H_6, the dissociation of H_2, and

the propyne hydrogenation pathway on Cu(1 1 1) and Ni(1 1 1). In addition, the eventual formation of carbide and hydride phases on the (sub-)surface of these metals under reaction conditions and possible routes for oligomerization were also investigated.

4.3.1. Adsorption of C_3H_4 and C_3H_6

Propyne is adsorbed very weakly on Cu(1 1 1), BE = −0.17 eV. This value is 0.5 eV smaller than previous computational estimates based on the PW91, although similar reduction of the binding energies of double and triple bonds on the metal surfaces have been found when improving the GGA description of the energy [9,56]. This is due to a complex balance between the bonding to the surface and the activation of the double (triple) bonds in the organic molecules [57]. On the most stable position, the C≡C bond is in contact with a bridge site and the carbon atoms in the -yne moiety are placed over fcc and hcp sites. In contrast, propene is endothermically adsorbed on Cu(1 1 1). On stepped Cu(2 1 1), propyne is exothermically adsorbed by BE = −0.36 eV, while no adsorption is found for propene. This result resembles what happens on Au nanoparticles [14] (C≡C adsorbs while C=C does not), and is the origin of the high thermodynamic selectivity of copper catalysts in partial alkyne hydrogenation. The beneficial role of copper dispersion is also clear from these calculations, since low-coordinated sites (steps) exhibit a higher thermodynamic factor. The thermodynamic factor can be defined as the difference between the binding energy of the triple bond and the double bond. On Ni(1 1 1), we have the fcc-hcp site and the binding energy of propyne is −1.51 eV and the C≡C bond sits on an fcc site, similar to Pd(1 1 1) [9]. The C=C bond of propene is thermoneutrally bonded to the bridge Ni due to the Pauli repulsion between the surface and the methyl group.

4.3.2. H_2 dissociation

Dissociation of molecular hydrogen on Cu(1 1 1) is marginally endothermic (0.16 eV) and is hindered by a large barrier of 0.83 eV. This is similar to what happens on Au nanoparticles [14] and is opposite to the barrier-free process on Pd(1 1 1) [58]. The poor activation of H_2 on Cu can be understood by the low position of the *d*-band with respect to the Fermi level and its high degree of filling [59]. In contrast, for very small and fluxional Cu clusters, exothermic reaction energies have been obtained [60]. Therefore H_2 activation on copper shows marked structure sensitivity. On Ni(1 1 1) dissociation is exothermic by −0.75 eV per H_2 molecule, in agreement with previous calculations [60]. The barrier for dissociation is 0.17 eV with respect to the gas phase, i.e. very low in comparison with that on copper.

4.3.3. Hydride and carbide formation

It is well known that application of high H_2 pressures over Ni and Pd lead to the formation of hydride phases [61,62]. These hydrides are highly active for alkyne hydrogenation but they are poorly selective to the alkene and mainly lead to over-hydrogenation [2,11,33,63]. The binding energy per H atom for both Cu(1 1 1) and Ni(1 1 1) slabs was calculated in order to understand the state of the metal surface when the hydrogen coverage gradually increases up to 3 ML (Fig. 12). The interaction energy for hydrogen adsorption is always more exothermic on Ni than on Cu. With the data above, the *ab initio* thermodynamics at 523 K for both metals has been generated (Fig. S7). While on Ni the formation of the subsurface layer takes place at $p(H_2)$ <1 bar, this is not observed for Cu. Only under very high hydrogen pressures the hydride phase is observed for Cu. This explains why for Ni unselective hydride structures appear at very low hydrogen-to-alkyne ratios while, Cu is more resistant to the formation of hydride layer (See Fig. 12).

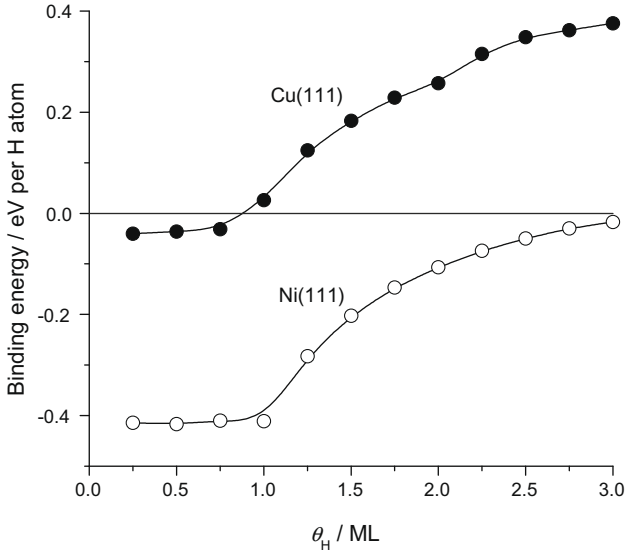

Fig. 12. Average binding energies of hydrogen atoms on Cu(1 1 1) and Ni(1 1 1) vs. the coverage.

Yet a final consideration regards the formation of carbide phases in these two materials. Insertion of C from the Ni(1 1 1) surface to the subsurface position is very exothermic (−1.5 eV), while is endothermic for Cu(1 1 1) (0.5 eV). This shows the relative inability of Cu to form carbide phases. Carbide phases are found to act positively in selectivity in Pd systems [11,33]. From our results a similar behavior is expected for Ni.

4.3.4. C_3H_4 hydrogenation

The energy profiles during sequential hydrogenation of propyne to propene over copper and nickel are shown in Fig. 13, involving

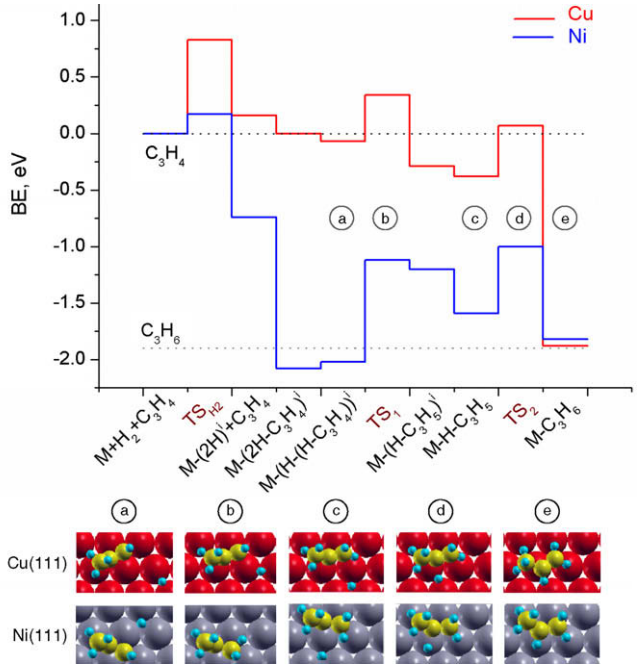

Fig. 13. Reaction energy profile for the hydrogenation of propyne to propene on Cu(1 1 1) and Ni(1 1 1). The schemes of the initial, transition state, and final steps are shown. The "i" label indicates that the fragments were calculated in independent unit cells.

the successive addition of atomic hydrogen to the substrate. The high barrier for H_2 dissociation on Cu(1 1 1) (0.83 eV) in comparison with Ni(1 1 1) (0.17 eV) can be readily observed. The hydrogenation of C_3H_4 to C_3H_6 on Cu(1 1 1) takes place through the activation of neighboring H atoms from fcc sites on the surface that are incorporated to the organic moiety. The first hydrogenation is weakly exothermic, by −0.22 eV and shows a very small barrier (0.41 eV). The second hydrogenation step is more exothermic (−1.51 eV) and shows an energy barrier of 0.45 eV. Once propene is formed it readily leaves the surface and therefore no further hydrogenation takes place. This is known as thermodynamic control and has been reported to be responsible for selectivity in Au nanoparticles [14], CO-poisoned Pd surfaces [9], and non-precious metal alloys [15].

On Ni(1 1 1), C_3H_4 adsorption is quite strong (−1.52 eV). The first hydrogen insertion from the clean surface is endothermic by 0.82 eV. At the transition state, the hydrogen atom is activated towards the top Ni center. The TS is over reactants by 0.89 eV. The second hydrogenation can take place in the terminal or the secondary carbons. For Ni the reaction on the secondary carbon to form propene is exothermic by 0.23 eV. Again the H atoms are activated over an on-top position and the barrier is 0.59 eV. As demonstrated in Fig. 12, Ni is more prone to generate subsurface H atoms. If the reaction takes place from the NiH_x hydride the atoms from the subsurface region present a chemical potential which is about 0.62 eV higher than those of surface, therefore these H atoms can attack either the primary or the secondary C atoms through much lower barriers leading to unselective hydrogenation processes.

4.3.5. Oligomerization

As a side product, carbon chains are formed both Cu and Ni. Based on the analysis of oligomers at the reactor outlet (Fig. S6), it can be inferred that the nature of green oil differs in the two metals and it depends on the experimental conditions for copper, but it is difficult to analyze experimentally due to the complex mixture produced. In order to shed light on oligomer formation, we have calculated the reaction path leading to C–C coupling of two different propyne molecules on the surface in a head-to-tail configuration (Fig. S8). For this we have employed a slightly different supercell $p(2 \times 4)$ reconstruction in which two propyne molecules have been placed along the long axis separated by at least 4 Å along this direction. These calculations do not account for all the possibilities for C–C coupling, since carbon–carbon bond formation can also take place from partially hydrogenated moieties. However, this is the simplest way to evaluate the ability of the surface in the formation of these bonds. On Cu(1 1 1) the polymerization is slightly endothermic by 0.28 eV, while it is endothermic by 0.83 eV on Ni. Consequently, the barrier for C–C coupling in a head-to-tail conformation is 1.01 eV on Cu while the value for Ni(1 1 1) is 1.49 eV. Thus, as experimentally observed, Cu surfaces are more prone to produce oligomers than Ni. This conclusion arises from both energetic and coverage effects since barriers are lower for oligomerization on Cu but also H coverage is smaller than in Ni, thus reducing the rate for hydrogenations.

However, on Cu for very dense propyne systems (two molecules in a $p(2 \times 2)$ reconstruction) the barrier for C–C coupling can be reduced to 0.4 eV, thus in agreement with the formation of benzene at 120 K described by Middleton and Lambert [64] that observed the formation of C_6 in TPD experiments at very lowtemperatures starting by an extremely compact organic surface layer. Finally, the ensemble needed for polymerization is larger than that of hydrogenation thus indicating why the propene selectivity is higher upon in well-dispersed Cu nanoparticles and after partial coking of the surface.

4.4. Comparison between experiments and DFT results

Different experimental observations can be correlated to the DFT results:

- For Cu-containing systems, the reaction rate is found to depend on the H_2 pressure with a reaction order of 1, while a value close to 0 is reported for the alkyne [21]. From the calculations, the larger barrier in Cu(1 1 1) is that of H_2 dissociation, thus this is the rate-determining step.
- Fortuitously the barriers for both rate-determining steps, H_2 dissociation on Cu(1 1 1) and first hydrogenation of propyne on Ni(1 1 1) show very similar reaction barriers. Thus the measured apparent barriers should be rather close in both systems explaining why the same temperature window can be employed in the reaction.
- Coming back to the results in Fig. 11, Ni(1 1 1) shows a sharp dependence on the H_2 pressure, while an almost constant behavior is found for Cu(1 1 1). At low H_2: alkyne ratios, the reaction is under stoichiometric conditions. At ratios > 1, the Ni(1 1 1) system tends to form hydrides, which cause a severe drop of the alkene selectivity. This can only be partially mitigated by the formation of the carbide, that effectively increases the selectivity window of Ni(111). For Cu the formation of the hydride is difficult and thus selectivity to propene is less dependent on the hydrogen-to-alkyne ratio.
- A final point regards the dependence of selectivity to propene with the temperature. For Ni, the C_3H_6 selectivity is quite independent of temperature. This is due to the preferential hydrogenation route and to the fact that H_2 splitting is not the rate-determining step. Once the more selective carbide phase is formed, its equilibrium with the hydride is the main controller of the alkene–alkane selectivity. In contrast for Cu a large dependence on temperature was found. This is because the leading reaction competition is between the formation of the alkene or the oligomer. Thus alkyne residence time on the surface and H coverages (which strongly depend on the temperature) are the two key factors affecting selectivity.
- The nature of oligomers on nickel and copper is substantially different. Oligomers on nickel are more complex, including short, long, as well as aromatic fractions, and contain carbon structures that are not divisible by three. The differences in the oligomeric compounds are due to the different C–C coupling barriers, but also to the ability of the metal to hydrogenate or to fragment C–C bonds at the steps.

5. Conclusions

Copper-based catalysts obtained by activation the Cu–Al hydrotalcite precursor proved highly active, selective, and stable in partial propyne hydrogenation. The hydrotalcite route confers beneficial properties to the final catalysts (high metal loading and exposed surface area), exceeding the performance of supported copper catalysts. Proper selection of the calcination temperature of the hydrotalcite precursor and reduction of the derived mixed oxide is decisive for the catalytic behavior, determining important properties in particular the copper dispersion. The best catalyst, calcined at 873 K and reduced at 573 K, displayed C_3H_6 selectivity slightly above 80% at full C_3H_4 conversion. The best activated Ni–Al hydrotalcite-derived in our previous work [16] led to similar propene selectivity under optimal conditions. However, the competing mechanisms are completely different. Propane was hardly observed over Cu catalysts (minimal production at H_2:C_3H_4 ratios >10, the other products being oligomer species),

while Ni produces substantial amounts propane at high partial H_2 pressures. Density Functional Theory provided further insight on the hydrogenation of propyne to propene on Cu and Ni. Bonding to the Cu surface is small for both reactants and the barriers for hydrogenation are also relatively small. After sequential hydrogenation the product C_3H_6 is not bonded to the surface. As for Au nanoparticles, the thermodynamic control is found. Moreover, the formation of subsurface hydride species on Cu is highly unlikely. For Ni, propyne is strongly adsorbed on the surface and hydride formation is important at relatively low H_2 pressures. The unselective hydride layer induces over-hydrogenation. Finally, oligomerization is another competing process that has mostly been neglected. We show how at low hydrogen pressures oligomerization might be the dominant process and it is easier for the systems with a smaller C affinity, i.e. Cu. Therefore in order to obtain selectivity for the hydrogenation of propyne in propyne-propene mixtures three processes need to be inhibited: adsorption of the desired product, formation of the metal hydride, and oligomerization.

Acknowledgments

This research was supported by the Spanish MICINN (CTQ2006-01562/PPQ, CTQ2009-098241PPQ, CTQ2006-004641BQU, Consolider-Ingenio 2010, grant CSD2006-0003), and the ICIQ Foundation

Appendix A. Supplementary data

Supplementary data associated with this article can be found, in the online version, at doi:10.1016/j.jcat.2009.10.019.

References

[1] M.L. Derrien, in: L. Červený (Ed.), Catalytic Hydrogenation Studies of Surface Science Catalysis, Elsevier, Amsterdam, 1986, p. 613.
[2] A. Borodziński, G.C. Bond, Catal. Rev. Sci. Eng. 48 (2006) 91.
[3] H.F. Rase, Handbook of Commercial Catalysts, CRC Press, United States, 2000. 105.
[4] N.A. Khan, S. Shaikhutdinov, H.-J. Freund, Catal. Lett. 108 (2006) 159.
[5] N. Semagina, A. Renken, L. Kiwi-Minsker, Chem. Eng. Sci. 62 (2007) 5344.
[6] Á. Mastalir, B. Rác, Z. Király, Á. Molnár, J. Mol. Catal. A: Chem. 264 (2007) 170.
[7] M. Ruta, N. Semagina, L. Kiwi-Minsker, J. Phys. Chem. C 112 (2008) 13635.
[8] O. Mekasuwandumrong, S. Somboonthanakij, P. Praserthdam, J. Panpranot, Ind. Eng. Chem. Res. 48 (2009) 2819.
[9] N. López, B. Bridier, J. Pérez-Ramírez, J. Phys. Chem. C 112 (2008) 9346.
[10] J.A. Anderson, J. Mellor, R.P.K. Wells, J. Catal. 261 (2009) 208.
[11] D. Teschner, J. Borsodi, A. Wootsch, Z. Révay, M. Hävecker, A. Knop-Gericke, S.D. Jackson, R. Schlögl, Science 320 (2008) 86.
[12] F. Studt, F. Abild-Pedersen, T. Bligaard, R.Z. Sørensen, C.H. Christensen, J.K. Nørskov, Angew. Chem., Int. Ed. 47 (2008) 9299.
[13] J.A. López-Sánchez, D. Lennon, Appl. Catal. A 291 (2005) 230.
[14] Y. Segura, N. López, J. Pérez-Ramírez, J. Catal. 247 (2007) 383.
[15] F. Studt, F. Abild-Pedersen, T. Bligaard, R.Z. Sorensen, C.H. Christensen, J.K. Nørskov, Science 320 (2008) 1320.
[16] S. Abelló, D. Verboekend, B. Bridier, J. Pérez-Ramírez, J. Catal. 259 (2008) 85.
[17] G.C. Bond, R.S. Mann, J. Chem. Soc. (1959) 3566.
[18] J.T. Wehrli, D.J. Thomas, M.S. Wainwright, D.L. Trimm, N.W. Cant, Appl. Catal. 66 (1990) 199.
[19] J.T. Wehrli, D.J. Thomas, M.S. Wainwright, D.L. Trimm, N.W. Cant, Appl. Catal. 70 (1991) 253.
[20] N.J. Ossipoff, N.W. Cant, J. Catal. 148 (1994) 125.
[21] R.A. Koeppel, J.T. Wehrli, M.S. Wainwright, D.L. Trimm, N.W. Cant, Appl. Catal. 120 (1994) 163.
[22] J.C. Rodriguez, A.J. Marchi, A. Borgna, E. Romeo, A. Monzón, Stud. Surf. Sci. Catal. 139 (2001) 37.
[23] S. Abelló, J. Pérez-Ramírez, Adv. Mater. 18 (2006) 2436.
[24] D. Briggs, M.P. Seah (Eds.), Practical Surface Analysis, Auger and X-Ray Photoelectron Spectroscopy, vol. 1, John Wiley and Sons, Chichester, 1994.
[25] J.W. Evans, M.S. Wainwright, A.J. Bridgewater, D.J. Young, Appl. Catal. 7 (1983) 75.
[26] G. Kresse, J. Hafner, Phys. Rev. B 47 (1993) 558.
[27] R.W.G. Wyckoff, Crystal Structures, Interscience, New York, 1965.
[28] H.J. Monkhorst, J.D. Pack, Phys. Rev. B 13 (1976) 5188.
[29] B. Hammer, L.B. Hansen, J.K. Nørskov, Phys. Rev. B 59 (1999) 7413.
[30] P.E. Blöchl, Phys. Rev. B 50 (1994) 17953.
[31] J. Horiuti, M. Polanyi, Trans. Faraday Soc. 30 (1934) 1164.
[32] G. Henkelman, B.P. Uberuga, H. Jonsson, J. Chem. Phys. 113 (2000) 99.
[33] A.D. Johnson, S.P. Daley, A.L. Utz, S.T. Ceyer, Science 257 (1992) 223.
[34] J. Greeley, W.P. Krekelberg, M. Mavrikakis, Angew. Chem., Int. Ed. 43 (2004) 4296.
[35] The chemical potential was calculated as the summation of the computed energy and zero point vibrational energies plus the pressure term and the thermal contribution to the enthalpy and the entropy taken from the tables of http://webbook.nist.gov/chemistry, retrieved August 2009.
[36] F. Cavani, F. Trifiro, A. Vaccari, Catal. Today 11 (1991) 173.
[37] S.R. Segal, K.A. Carrado, C.L. Marshall, K.B. Anderson, Appl. Catal. A 248 (2003) 33.
[38] A. Alejandre, F. Medina, P. Salagre, X. Correig, J.E. Sueiras, Chem. Mater. 11 (1999) 939.
[39] S. Kannan, V. Rives, H. Knozinger, J. Solid State Chem. 177 (2004) 319.
[40] L.H. Zhang, C. Zheng, F. Li, D.G. Evans, X. Duan, J. Mater. Sci. 43 (2008) 237.
[41] S. Abelló, F. Medina, D. Tichit, J. Pérez-Ramírez, J.C. Groen, J. Sueiras, P. Salagre, Y. Cesteros, Chem. Eur. J. 11 (2005) 728.
[42] Substitutional energies on oxides have been calculated according to the following reaction: MO + Al → MAlO + MO, M = Cu or Ni. Bulk oxide calculations were performed in a $(2 \times 2 \times 2)$ configuration where a Cu (Ni) atom was substituted by Al. For Ni, a GGA + U scheme has been employed with $U = 6.3$, $J = 1.0$ as indicated in F. Cinquini, L. Giordano, G. Pacchioni, A.M. Ferrari, C. Pisani, C. Roetti, Phys. Rev. B 74 (2006) 165403.
[43] J.M. Dumas, C. Geron, A. Kribii, J. Barbier, Appl. Catal. 47 (1989) L9.
[44] Z. Jiang, Z. Hao, J. Yu, H. Hou, C. Hu, J. Su, Catal. Lett. 99 (2005) 157.
[45] W.-P. Dow, Y.-P. Wang, T.-J. Huang, Appl. Catal. A 190 (2000) 25.
[46] N.S. McIntyre, M.G. Cook, Anal. Chem. 47 (1975) 2208.
[47] K.S. Kim, J. Electron Spectrosc. Relat. Phenom. 3 (1974) 217.
[48] E. Paparazzo, Appl. Surf. Sci. 25 (1986) 1.
[49] B.R. Strohmeier, D.E. Leyden, R.S. Field, D.M. Hercules, J. Catal. 94 (1985) 514.
[50] P.H. Bolt, F.H.P.M. Habraken, J.W. Geus, J. Solid State Chem. 135 (1998) 59.
[51] M.P. Seah, G.C. Smith, M.T. Anthony, Surf. Interf. Anal. 15 (1990) 293.
[52] These calculations were performed as follows. The (1 1 1) surfaces of Cu and CuO were prepared. For the oxide a stoichiometric surface arises. Segregation energies were calculated as $E_{seg} = E(Al_s \text{ at CuX}) - E(Al_{subs} \text{ at CuX})$ where 's' indicates surface and 'subs' the near-to-surface layer and 'X' stands for the metal or the oxide. Supercells employed lead to an Al fraction of about 0.05. The corresponding differential segregation energy was calculated as $\Delta E_{seg} = E_{seg}(\text{Al at Cu}) - E_{seg}(\text{Al at CuO})$.
[53] J. Wood, M.J. Alldrick, J.M. Winterbottom, E.H. Stitt, S. Bailey, Catal. Today 128 (2007) 52.
[54] G. Socrates, Infrared and Raman Characteristic Group Frequencies, John Wiley and Sons, New York, 2001.
[55] R.T. Vang, K. Honkala, S. Dahl, E.K. Vestergaard, J. Schnadt, E. Lægsgaard, B.S. Clausen, J.K. Nørskov, F. Besenbacher, Nat. Mater. 4 (2005) 160.
[56] J. Andersin, N. Lopez, K. Honkala, J. Phys. Chem. C 113 (2009) 8278.
[57] A. Valcárcel, A. Clotet, F. Illas, J.M. Ricart, Phys. Chem. Chem. Phys. 122 (2000) 7573.
[58] N. Lopez, Z. Łodziana, F. Illas, M.B. Salmeron, Phys. Rev. Lett. 93 (2004) 146103.
[59] B. Hammer, J.K. Nørskov, Nature 376 (1995) 238.
[60] N. Lopez, F. Illas, G. Pacchioni, J. Phys. Chem. B 103 (1999) 8552.
[61] B. Baranowski, S.M. Filipek, J. Alloys Compd. 404–406 (2005) 2–6.
[62] V. Azambuja, S. Miraglia, D. Fruchart, S. Tavares, D. dos Santos, M. Mezouar, J. Alloys Compd. 404–406 (2005) 77–81.
[63] G. Henkelman, A. Arnaldsson, H. Jonsson, J. Chem. Phys. 124 (2006) 044706.
[64] R. Middleton, R.M. Lambert, Catal. Lett. 59 (1999) 15.